Ann. Geophys., 25, 1311–1322, 2007
www.ann-geophys.net/25/1311/2007/

Annales Geophysicae

Wavelength dependence of the linear growth rate of the E_s layer instability

R. B. Cosgrove

Center for Geospace Studies, SRI International, Menlo Park, California, USA

Received: 16 August 2006 – Revised: 2 May 2007 – Accepted: 28 May 2007 – Published: 29 June 2007

Abstract. It has recently been shown, by computation of the linear growth rate, that midlatitude sporadic-E (E_s) layers are subject to a large scale electrodynamic instability. This instability is a logical candidate to explain certain frontal structuring events, and polarization electric fields, which have been observed in E_s layers by ionosondes, by coherent scatter radars, and by rockets. However, the original growth rate derivation assumed an infinitely thin E_s layer, and therefore did not address the short wavelength cutoff. Also, the same derivation ignored the effects of F region loading, which is a significant wavelength dependent effect. Herein is given a generalized derivation that remedies both these short comings, and thereby allows a computation of the wavelength dependence of the linear growth rate, as well as computations of various threshold conditions. The wavelength dependence of the linear growth rate is compared with observed periodicities, and the role of the zeroth order meridional wind is explored. A three-dimensional paper model is used to explain the instability geometry, which has been defined formally in previous works.

Keywords. Ionosphere (Mid-latitude ionosphere; Plasma waves and instabilities; Ionosphere irregularities)

1 Introduction

Cosgrove and Tsunoda (2002) showed that the equilibrium configuration of a midlatitude sporadic-E (E_s) layer at a wind shear node is unstable, at night, to electrodynamical forces that arise when plane wave perturbations in altitude or field-line-integrated (FLI) density are imposed on the E_s layer. This instability is a logical candidate to explain certain frontal structuring events in E_s layers, which have been observed over the years by ionosonde, and by coherent scatter radars (Tsunoda et al., 2004). Most revealing in this regard is the fact that the observed structures strongly prefer the same skewed azimuthal alignment that maximizes the growth rate of the instability. The instability is also a potential source of large polarization electric fields in E_s layers, which have been indicated by coherent radar backscatter (e.g., Schlegel and Haldoupis, 1994; Tsunoda et al., 1994), and measured in situ during the two SEEK rocket campaigns (Fukao et al., 1998; Pfaff et al., 1998, 2005; Yamamoto et al., 2005). However, the derivation given by Cosgrove and Tsunoda (2002) assumed an infinitely thin E_s layer, and therefore did not address the short wavelength cutoff of the instability. Also, the same derivation assumed $\frac{\Sigma_H}{\Sigma_P} \gg 1$, where Σ_H is the FLI Hall conductivity of the E_s layer, and $\Sigma_P = \Sigma_{PE} + \Sigma_L$ is the effective FLI Pedersen conductivity, due to F layer loading (Σ_L), and due to the E_s layer itself (Σ_{PE}). This assumption means, essentially, that F region loading is ignored. Herein is given a generalized derivation that removes both these assumptions, and thereby allows a computation of the wavelength dependence of the linear growth rate, as well as computations of various threshold conditions. Various ramifications of the linear growth rate behavior are explored.

Specifically, the derivation given by Cosgrove and Tsunoda (2002) is generalized to an equilibrium configuration of a finite thickness E_s layer with compressional wind shear forces balanced by outward diffusion, and wavelength dependent mapping of electric fields to the F layer (where they are loaded). The F layer is assumed to be stable, which is in contradistinction to F layer assumptions made by Cosgrove and Tsunoda (2004a, b, 2006), when they treated the long wavelength interaction between the Perkins instability (Perkins, 1973) and the E_s layer instability. The resulting theory agrees exactly with the original theory at long wavelengths, with $\Sigma_L = 0$, but finds a short wavelength cutoff that depends on the equilibrium layer thickness (or equivalently, the wind shear). More completely, the threshold for stability depends on multiple parameters, including at least the

Correspondence to: R. B. Cosgrove
(russell.cosgrove@sri.com)

Published by Copernicus Publications on behalf of the European Geosciences Union.

wavelength, the equilibrium layer thickness, $\frac{\Sigma_H}{\Sigma_P}$, and the (effective) eastward electric field. The effect of wavelength dependent mapping of the electric field to the F layer, and the associated electrical loading, creates a growth rate maxima at a wavelength just above the cutoff.

It is necessary to know the short-wavelength cutoff of the E_s layer instability in order to study plasma structuring at scales above the long-wavelength cutoff of the gradient drift instability (in E_s layers). Hysell et al. (2002) discovered (theoretically) an instability applicable to midlatitude E_s layers which has a preferred scale of around 1 km. This scale (1 km) is above the long-wavelength cutoff of the gradient drift instability (Tsunoda et al., 1994; Kelley and Gelinas 2000; Rosado-Román et al., 2004; and Seyler et al, 2004), and we find herein that it is below the short-wavelength cutoff of the E_s layer instability. Spectral measurements from the SEEK and SEEK-2 rocket campaigns (Mori and Oyama, 1998; Pfaff et al., 2005) cover this transition scale region.

Spaced ionosonde observations (Goodwin and Summers, 1970) have revealed the consistent presence of frontal structures in Southern Hemisphere E_s layers, with fronts elongated from northwest to southeast. Cosgrove and Tsunoda (2002) noted that this orientation points to the E_s layer instability as source. Goodwin and Summers (1970) found that the (horizontal) wavelength range for the frontal structures was 10–40 km, with a mean of 24 km. Below we will consider whether this wavelength range is also consistent with an E_s layer instability source, and find in the affirmative.

The coherent radar backscatter from E_s layers known as QP echoes (Yamamoto et al., 1991) has also been found to form frontal structures with a preferred orientation matching that of the E_s layer instability (Yamamoto et al., 1994, 1997; Hysell, 2006). By examining range profiles of QP echo Doppler velocity presented by various authors, a wavelength in the perpendicular to $\boldsymbol{B}$ direction can be inferred. From Yamamoto et al. (1991), we estimate 8 km. From Tsunoda et al. (1998), we estimate 18 km. From Yamamoto et al. (1998), we estimate 24 km. We can also use the interferometry results of Riggin et al. (1986), from which we estimate 18 km. (Note that in all cases we are estimating the wavelength along the $\hat{y}'$ direction of Cosgrove and Tsunoda (2002, 2003), which is what is applicable to the theory below, and described in Sect. 2.) Putting these estimates together we find a wavelength range of 8–24 km, with a mean of 17 km. Hence, the estimated wavelength for QP echoes is slightly, but not significantly less than the estimated wavelength for ionosonde observed frontal structures.

Finally, we give a few cautionary remarks regarding the interpretation of this paper. The linear growth rate, in general, applies to the growth of small perturbations about an equilibrium configuration. Because of possible time variation of the wind profile, there is some doubt about whether the equilibrium configuration assumed herein will ever be obtained (Jones, 1989). This fact colors the interpretation of the results, and one possible effect is discussed in Sect. 5. The equilibrium configuration considered here is valid below about 110 km in altitude. Above 110 km the meridional wind affects the layer altitude, and the meridional shear (which we do not include) plays a role in establishing the equilibrium (Whitehead, 1970). Conclusions with respect to wavelength dependance of observed phenomena based on the linear growth rate dependance are in turn based on the idea that seed excitations are present equally at all wavelengths. The seed excitations are most likely perturbations in the neutral wind profile, associated with gravity waves (propagating (Huang and Kelley, 1996), or breaking (Yokoyama et al., 2004)), or with a Kelvin Helmholtz instability of the neutral shear (Larsen, 2000; Bernhardt, 2002). The spectrum of these processes will contribute to the wavelength dependance of the observed phenomena. Finally, the nonlinear response, specifically at what amplitude wave growth saturates, will also play an important role in determining the wavelength dependance.

The paper begins in Sect. 2 with description of the problem geometry using a three-dimensional paper model. Section 3 describes the instability action in simplest possible form, using the paper model of Sect. 2. Section 4.1 gives the derivation of the equilibrium configuration. Section 4.2 gives the derivation of the growth rate. Section 5 gives analysis of the derived growth rate, and forms conclusions. Section 5 also explains how to generalize the results to situations with background electric fields. Section 6 summarizes the results.

2 Geometry and coordinates

The basic geometry of the unstable modes of the E_s layer instability in the Northern Hemisphere is explained in Fig. 1. The pink and purple strips represent sheets of ionization elongated along the northwest to southeast axis, with a relative altitude displacement. The pink strip is at an altitude of 106 km; the purple strip at 104 km; and the inner edges of the strips are connected by magnetic field lines. The white strip that connects the inner edges of the colored strips does not represent plasma; it merely represents the plane of magnetic field lines that connect the inner edges of the plasma strips, and serves as a surface on which to draw the x, x', and z' coordinate axes.

Figure 1 is a schematic depiction of the unstable modes (waves) of the E_s layer instability in the Northern Hemisphere. The waves are two-dimensional, with a symmetry direction which we denote $\hat{x}$. Specifically, the symmetry direction is along the wave phase fronts, and horizontal. In Fig. 1 the symmetry direction is to the northwest, as an example, but will be taken as a variable below. We define a primed coordinate system as shown in Fig. 1, with $\hat{z}'$ along the magnetic field $\boldsymbol{B}$, $\hat{y}'$ perpendicular to both $\hat{x}$ and $\hat{z}'$, and $\hat{x}'=\hat{y}'\times\hat{z}'$. The pencil indicates the direction of $\hat{y}'$, and we use the figure to define the orientation of the coordinate system. It is evident from Fig. 1 that the x' axis is connected to

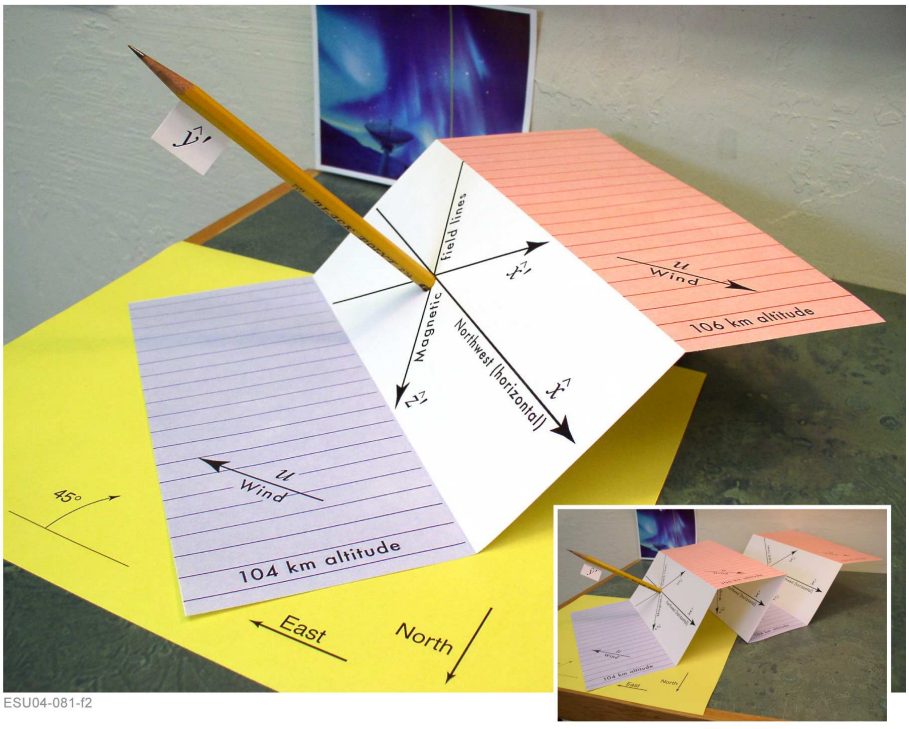

Fig. 1. Three-dimensional view of the E_s layer instability geometry.

the x axis by the magnetic field lines. Therefore, the $\hat{x}'$ direction is a symmetry direction for FLI quantities, and – under the assumption that the electric field $\boldsymbol{E}$ maps unattenuated along $\boldsymbol{B}$ – for $\boldsymbol{E}$ also. By integrating along $\boldsymbol{B}$ we will obtain below a one-dimensional system of FLI quantities (moments), together with the electric field, which contains the essential dynamics of the E_s layer instability. This system is analogous to the system of moments defined by Perkins (1973), which contains the essential dynamics of the Perkins instability.

To round out our notation we define a few additional quantities not shown in Fig. 1. The $\hat{z}$ direction will be taken as vertically downward, with $\hat{y}=\hat{z}\times\hat{x}$ completing a right handed system. The angle between the symmetry direction $\hat{x}$ and the northward, or equivalently between $\hat{y}$ and the eastward, will be denoted θ, where we take θ to be positive for the azimuthal orientation shown in Fig. 1. (Figure 1 shows the special case θ=45°.) However, for mathematical convenience we will use the angle θ' between $\hat{y}'$ and the eastward, to define the azimuthal orientation of the symmetry direction. Using the fact that the symmetry direction $\hat{x}$ is constrained to be horizontal, it is straightforward to show that $\tan\theta = \tan\theta' \cos\theta''$, where θ'' is the complement of the magnetic dip angle. These definitions are the same as those given by Cosgrove and Tsunoda (2002, 2003), and it is hoped that Fig. 1 will ease the task of visualizing the geometry, and the coordinate systems that are natural to it.

Figure 1 shows a westward wind at 106 km in altitude, and an eastward wind at 104 km. In general we choose a wind field $\boldsymbol{u}$ with a constant meridional component u_N, and a zonal component uz that varies linearly with altitude, where u is the wind shear, and z is the altitude (positive downward). Specifically,

$$\begin{aligned}\boldsymbol{u} &= uz\hat{e} + u_N\hat{n} \\ &= (u_N\cos\theta'\cos\theta'' - uz\sin\theta')\hat{x}' \\ &+ (u_N\sin\theta'\cos\theta'' + uz\cos\theta')\hat{y}' \\ &+ u_N\sin\theta''\hat{z}', \end{aligned} \quad (1)$$

where $\hat{e}$ and $\hat{n}$ are eastward and northward, respectively. The wind shear u is positive for the configuration of Fig. 1. The wind field (Eq. 1) is an approximation to a rotational wind shear, in the vicinity of the E_s layer equilibrium altitude in the lower E region, which is at the zero of the zonal wind (see discussion below). At higher altitudes the meridional shear becomes important, and therefore use of the wind field (Eq. 1) limits the applicability of this work to the lower E region.

3 Instability description in simplest case

We begin by describing the vertical equilibrium of an E_s layer. Assuming the winds to be horizontal, and no significant electric fields, the dominant contributor to vertical

motion in the lower E region steady-state ion velocity equation is the term $\boldsymbol{u}\times\boldsymbol{B}/(\rho_i B)$, where ρ_i is the ratio of the ion-neutral collision frequency to the ion gyro frequency, and $\boldsymbol{B}=B\hat{z}'$ is the magnetic field. By "dominant" we mean that other terms with vertical components are smaller by a factor $1/\rho_i$, and $\rho_i \gg 1$ in the lower E region. For the meridional wind, $\boldsymbol{u}\times\boldsymbol{B}$ is horizontal. However, for a westward (eastward) directed wind, $\boldsymbol{u}\times\boldsymbol{B}$ has a downward (upward) component. Hence, in the lower E region, when there are no background electric fields, plasma collects almost exactly at the zero of the zonal component of the neutral wind, with a westward wind above and an eastward wind below (Whitehead, 1970). (Section 5 describes how to extend this analysis when there is a background electric field.) In Fig. 1, the equilibrium altitude is 105 km.

Consider the stability of the altitude perturbation shown in Fig. 1, where the pink strip of plasma has been slide along $\boldsymbol{B}$ up to 106 km, and the blue strip of plasma has been slid down along $\boldsymbol{B}$ to 104 km. The inset in Fig. 1 shows how the two-strip configuration can be cascaded ad-infinitum, to form a skewed-square-wave modulation of the layer altitude. We assume in this example that there is no meridional wind (u_N=0). Therefore, as shown in the figure, the raised strip sees a westward wind, and the lowered strip an eastward wind, so that the collisional ions are driven away from the white plane containing the $\boldsymbol{B}$-field lines that connect the inner edges of the strips. However, the magnetized (non-collisional) electrons are not effected by the wind and remain behind, forming a layer of charge on the white plane, which under the assumption that the conductance is infinite along $\boldsymbol{B}$, and that the strips are infinitely long, becomes an infinite sheet of charge of thickness d. As the thickness d grows, a polarization electric field builds up, which is directed toward, and perpendicular to, the sheet charge. That is, the electric field on the pink layer side of the sheet charge is in the $\hat{y}'$ direction, and the electric field on the purple layer side of the sheet charge is in the $-\hat{y}'$ direction. This can be further argued by noting that the polarization field must be perpendicular to $\boldsymbol{B}$, and perpendicular to the symmetry direction $\hat{x}$, the latter because charge density must be invariant under translations in the symmetry direction.

The polarization electric field builds up until the wind-driven ion drift along $\hat{y}'$ is canceled by electric-field-driven Pedersen drift. The only remaining ion motion is the wind-driven ion drift along $\hat{x}'$, which remains completely unchecked. (Note that the wind is everywhere perpendicular to $\hat{z}'$.) Therefore, the pink plasma strip will slide away from the equilibrium altitude along $\hat{x}'$, and the purple plasma strip will slide away from the equilibrium altitude along $-\hat{x}'$, that is, the equilibrium configuration is unstable to the perturbation shown in Fig. 1.

If the entire configuration of Fig. 1 is rotated 90° about the vertical, so that $\hat{x}$ is directed toward the northeast, then the component of the wind driven ion drift along $\hat{x}'$ changes sign, and the plasma strips drift back to the equilibrium altitude. That is, the configuration is stable. It is also easy to verify that the configuration is stable if $\hat{x}$ is either meridional, or zonal. Therefore, the process predicts a unique orientation for unstable waves, which matches the observed orientation for E_s layer frontal structures in the Northern Hemisphere. In the Southern Hemisphere the stable and unstable orientations are interchanged.

The growth rate for the instability process just described was derived by Cosgrove and Tsunoda (2002) as

$$\lambda = u \sin\theta' \cos\theta' \sin\theta'' \frac{\sigma_H}{\rho_i \sigma_P}, \tag{2}$$

where σ_H and σ_P are the Hall and Pedersen conductivities, respectively, at the altitude of the (assumed thin) E_s layer. The θ' dependence in Eq. (2) determines the orientation that maximizes the growth rate. The derivation by Cosgrove and Tsunoda (2002) also included a zeroth order meridional Hall current, which is found to be important below, but which is not accounted for in the expression (2).

The above description explains the simplest possible conception of the E_s layer instability. However, the simplifications involved preclude consideration of the following very important elements:

1. The F layer constitutes an additional electrical load on the E_s layer generated polarization electric fields, which greatly reduces their strength. This is a wavelength dependent effect, due to the wavelength dependence of electric field mapping along $\boldsymbol{B}$.

2. A meridional wind (u_N) can drive a strong meridional current (a Hall current) in the E_s layer, which was found by Cosgrove and Tsunoda (2004a) to greatly enhance the growth rate of the E_s layer instability in the presence of an F-layer electrical load. This effect occurs because modulations in FLI density become coupled to altitude modulations.

3. When the thickness of the E_s layer approaches the perturbation wavelength, it is evident from Fig. 1 that the simple considerations employed in the description above begin to break down.

Item-3 has not been addressed by previous derivations of the linear growth rate, and analysis of the other effects has been quite limited. Therefore, we now proceed to a more complete derivation of the linear growth rate that includes all these effects.

4 Growth rate for thick E_s layer

4.1 Equilibrium configuration

We begin by deriving the horizontally uniform equilibrium plasma configuration in the wind field (Eq. 1), assuming that

generation, recombination, and gravity can be ignored. Horizontal uniformity means that all quantities – such as the charge density and current – must be invariant under horizontal translations. Therefore, the plasma density gradient and electric field must be vertical, and in steady state the vertical current must be zero. The steady state ion and electron velocity equations can be written in the form

$$\begin{aligned}
&\frac{1}{\Lambda_i}\boldsymbol{v}_i = \boldsymbol{F}_{i\perp} + \frac{1}{\rho_i}\boldsymbol{F}_i \times \hat{b} + \frac{\boldsymbol{F}_{i\parallel}}{\Lambda_i},\\
&\frac{1}{\Lambda_e}\boldsymbol{v}_e = \boldsymbol{F}_{e\perp} - \frac{1}{\rho_e}\boldsymbol{F}_e \times \hat{b} + \frac{\boldsymbol{F}_{e\parallel}}{\Lambda_e}, \quad \text{where}\\
&\boldsymbol{F}_i = \frac{\boldsymbol{E}}{B\rho_i} + \boldsymbol{u} - \frac{T}{eB\rho_i}\frac{\nabla n}{n},\ \Lambda_i = \frac{\rho_i^2}{\rho_i^2+1},\\
&\boldsymbol{F}_e = \frac{-\boldsymbol{E}}{B\rho_e} + \boldsymbol{u} - \frac{T}{eB\rho_e}\frac{\nabla n}{n},\ \Lambda_e = \frac{\rho_e^2}{\rho_e^2+1},
\end{aligned} \tag{3}$$

where ρ_i (ρ_e) is the ratio of the ion-neutral (electron-neutral) collision frequency to the ion (electron) gyro frequency, e is the absolute value of the charge on an electron, T is the temperature under the isothermal assumption ($T{=}T_i{=}T_e$), B is the magnetic field magnitude, $\hat{b}$ is a unit vector in the magnetic field direction, $\boldsymbol{E}$ is the electric field, n is the plasma density under the quasi-neutral assumption ($n{=}n_i{=}n_e$), and $\boldsymbol{v}_i$ ($\boldsymbol{v}_e$) is the ion (electron) velocity. To get the equilibrium electric field we set the vertical current to zero ($J_z{=}en(v_{iz}{-}v_{ez}){=}0$), using Eqs. (3) and (1), and solve for the electric field, which gives

$$\begin{aligned}
\boldsymbol{E}_{n_0} = &\\
&\hat{z}\frac{-T}{eBn_0G}\frac{\partial n_0}{\partial z}[(\frac{\Lambda_e}{\rho_e}-\frac{\Lambda_i}{\rho_i})\sin^2\theta''+(\frac{1}{\rho_e}-\frac{1}{\rho_i})\cos^2\theta'']\\
&+\hat{z}(\Lambda_i-\Lambda_e)\frac{u_N}{G}\sin\theta''\cos\theta''+\hat{z}(\frac{\Lambda_i}{\rho_i}+\frac{\Lambda_e}{\rho_e})\frac{u}{G}z\sin\theta'',
\end{aligned}$$

where

$$G = \frac{1}{B}[(\frac{\Lambda_e}{\rho_e}+\frac{\Lambda_i}{\rho_i})\sin^2\theta''+(\frac{1}{\rho_e}+\frac{1}{\rho_i})\cos^2\theta''], \tag{4}$$

and where n_0 is the equilibrium plasma density distribution. As long as $\frac{\rho_i}{\rho_e}\cos^2\theta'' \gg 1$ (i.e., as long as the magnetic field lines are not horizontal), the last term is negligible when Eq. (4) is used in the ion velocity equation (3), and therefore we drop it. Similarly, as long as the magnetic field lines are not horizontal, the remaining terms are well approximated by

$$\begin{aligned}
\boldsymbol{E}_{n_0} &\cong \hat{z}\frac{-T}{en_0}\frac{\partial n_0}{\partial z} + \hat{z}B\rho_e u_N\tan\theta''\\
&= \frac{-T}{en_0}\nabla n_0 + \hat{z}B\rho_e u_N\tan\theta''.
\end{aligned} \tag{5}$$

The term $\frac{-T}{en_0}\nabla n_0$ is commonly referred to as an ambipolar electric field, which more generally takes the form $\frac{-T}{en}\nabla n$, for a plasma density n. The general form $\frac{-T}{en}\nabla n$ applies strictly only to an unmagnetized plasma, but as evidenced by the reduction of Eq. (4) to Eq. (5), is usually a good approximation for a magnetized plasma, as long as the geometry is not elongated along $\boldsymbol{B}$. This motivates that we consider

$$\boldsymbol{E}_0 = \frac{-T}{en}\nabla n + \hat{z}B\rho_e u_N\tan\theta'' \tag{6}$$

as the zeroth order electric field, about which we apply a first order perturbation analysis, so that perturbations in the ambipolar electric field (which does not map along $\boldsymbol{B}$) are included in the zeroth order field. Examining Eq. (3) reveals that assuming a zeroth order electric field of the form (6) in the ion velocity equation is equivalent to doubling the temperature, and adding a small constant vertical wind component $\frac{\rho_e}{\rho_i}u_N\tan\theta''\hat{z}$.

We now use the result (Eq. 6) to derive the equilibrium layer profile. Setting $v_{iz}{=}0$ and using Eq. (3) with Eq. (6) gives

$$\begin{aligned}
0 = v_{iz} &= (1-\Lambda_i)u_N\sin\theta''\cos\theta'' - \frac{\Lambda_i}{\rho_i}uz\sin\theta''\\
&-(\Lambda_i\sin^2\theta''+\cos^2\theta'')\frac{2T}{eB\rho_i n_0}\frac{\partial n_0}{\partial z}+\frac{\rho_e}{\rho_i}u_N\tan\theta''.
\end{aligned} \tag{7}$$

The Gaussian profile

$$n_0 = A_{00}\frac{b}{\sqrt{\pi}}\mathrm{e}^{-b^2(z-\bar{z}_0)^2} \tag{8}$$

satisfies Eq. (7) with

$$\bar{z}_0 = \frac{u_N}{u}(\frac{\cos\theta''}{\rho_i}+\frac{\rho_e}{\cos\theta''}),\ \text{ and }\ b^2 = \frac{eBu\sin\theta''}{4T}, \tag{9}$$

where A_{00} is a constant, and where we have set $\Lambda_i{=}1$ in the final result, which in the lower E region is valid to second order in $\frac{1}{\rho_i}$. Equations (8) and (9) give the equilibrium E_s layer profile.

4.2 Linearized equations of motion

In general form, the E_s layer instability involves the moments of an E_s layer taken along $\boldsymbol{B}$, in the wind field (Eq. 1), with electrical loading due to partial mapping of E_s layer generated polarization electric fields to the F layer. Specifically, we define the moments as

$$\begin{aligned}
&A_l = \int dz'\, n(z-\bar{z}h_{l1})^l \text{ where}\\
&h_{lk} = \begin{cases} 0 & l=k \\ 1 & \text{otherwise} \end{cases} \text{ and } \bar{z} = A_1/A_0,
\end{aligned} \tag{10}$$

where dz' denotes integration along the magnetic field, z is the altitude (positive downward), and n is the E_s layer plasma density distribution. The values of ρ_i and ρ_e (which appear under the integral $\int dz'$ in the equation of motion for A_l) will be approximated as the values at the equilibrium altitude of the E_s layer. (Note that the F layer would appear stable

under this approximation (no Perkins instability), whereas in the case of the E_s layer the effect of the variation of the wind velocity with altitude completely dominates the effects of the variations of the collision frequencies with altitude.) To follow this section it is important that the reader first read Sect. 2, which contains a discussion of the geometry and a definition of the coordinate system and other quantities to be used in the derivation below.

The equation of motion for the lth moment is derived as

$$\begin{aligned}
&\frac{\mathrm{d}A_l}{\mathrm{d}t} = \frac{\mathrm{d}}{\mathrm{d}t}\int \mathrm{d}z'\, n(z-\bar{z}h_{l1})^l \\
&= \int \mathrm{d}z'\, \frac{\mathrm{d}n}{\mathrm{d}t}(z-\bar{z}h_{l1})^l - \int \mathrm{d}z'\, nl(z-\bar{z}h_{l1})^{l-1}\frac{\mathrm{d}\bar{z}}{\mathrm{d}t}h_{l1} \\
&= -\int \mathrm{d}z'\, (\nabla\cdot n\boldsymbol{v}_i)(z-\bar{z}h_{l1})^l - l\frac{\mathrm{d}\bar{z}}{\mathrm{d}t}h_{l1}h_{l2}A_{l-1} \\
&= -\int \mathrm{d}z'\, [\nabla\cdot(n\boldsymbol{v}_i(z-\bar{z}h_{l1})^l) - n\boldsymbol{v}_i\cdot\nabla(z-\bar{z}h_{l1})^l] \\
&- l\frac{\mathrm{d}\bar{z}}{\mathrm{d}t}h_{l1}h_{l2}A_{l-1}, \qquad (11)
\end{aligned}$$

where the third equality uses the ion continuity equation, with $\boldsymbol{v}_i$ the ion velocity, and the fourth equality uses integration by parts.

Using the geometric relationship

$$z = -x'\cos\theta'\sin\theta'' - y'\sin\theta'\sin\theta'' + z'\cos\theta'' \qquad (12)$$

in Eq. (11) gives

$$\begin{aligned}
\frac{\mathrm{d}A_l}{\mathrm{d}t} &= -l\frac{\mathrm{d}\bar{z}}{\mathrm{d}t}h_{l1}h_{l2}A_{l-1} \\
&- \frac{\partial}{\partial y'}\int \mathrm{d}z'\, nv_{iy'}(z-\bar{z}h_{l1})^l \\
&- \cos\theta'\sin\theta''\int \mathrm{d}z'\, nv_{ix'}l(z-\bar{z}h_{l1})^{l-1} \\
&- (\sin\theta'\sin\theta'' + \frac{\partial\bar{z}}{\partial y'}h_{l1})\int \mathrm{d}z'\, nv_{iy'}l(z-\bar{z}h_{l1})^{l-1} \\
&+ \cos\theta''\int \mathrm{d}z'\, nv_{iz'}l(z-\bar{z}h_{l1})^{l-1}, \qquad (13)
\end{aligned}$$

where we have used the fact that FLI quantities are invariant under translations in the $\hat{x}'$ direction.

Using the steady state ion velocity equation (3) along with the assumed form (1) for the neutral wind field we obtain the following for the ion velocity components:

$$\begin{aligned}
\frac{1}{\Lambda_i}v_{ix'} &= u_N\cos\theta''(\cos\theta' + \frac{1}{\rho_i}\sin\theta') \\
&- uz(\sin\theta' - \frac{1}{\rho_i}\cos\theta') + \frac{E_{x'}}{B\rho_i} \\
&- \frac{T}{eB\rho_i n}(\frac{\partial n}{\partial x'} + \frac{1}{\rho_i}\frac{\partial n}{\partial y'}) + \frac{E_{y'}}{B\rho_i^2}, \\
\frac{1}{\Lambda_i}v_{iy'} &= u_N\cos\theta''(\sin\theta' - \frac{1}{\rho_i}\cos\theta') \\
&+ uz(\cos\theta' + \frac{1}{\rho_i}\sin\theta') - \frac{E_{x'}}{B\rho_i^2} \\
&- \frac{T}{eB\rho_i n}(\frac{\partial n}{\partial y'} - \frac{1}{\rho_i}\frac{\partial n}{\partial x'}) + \frac{E_{y'}}{B\rho_i}, \\
v_{iz'} &= u_N\sin\theta'' + \frac{E_{z'}}{B\rho_i} - \frac{T}{eB\rho_i n}\frac{\partial n}{\partial z'}, \qquad (14)
\end{aligned}$$

where the subscripts identify the components of the vector quantities.

In addition, we need the relations

$$\begin{aligned}
&\int \mathrm{d}z'\, (z-\bar{z}h_{l1})^l\frac{\partial n}{\partial x'} = \cos\theta'\sin\theta''lA_{l-1}h_{l2}, \\
&\int \mathrm{d}z'\, (z-\bar{z}h_{l1})^l\frac{\partial n}{\partial y'} = \\
&\frac{\partial A_l}{\partial y'} + (\sin\theta'\sin\theta'' + \frac{\partial\bar{z}}{\partial y'}h_{l1})lA_{l-1}h_{l2}, \\
&\int \mathrm{d}z'\, (z-\bar{z}h_{l1})^l\frac{\partial n}{\partial z'} = -\cos\theta''lA_{l-1}h_{l2}, \qquad (15)
\end{aligned}$$

which can be derived using Eqs. (12) and (10).

We consider first the equilibrium condition

$$\frac{\mathrm{d}A_l}{\mathrm{d}t} = 0,\ \frac{\partial A_l}{\partial y'} = 0,\ \boldsymbol{E} = \boldsymbol{E}_0. \qquad (16)$$

Substituting Eqs. (14), (15), (16), and (6) into Eq. (13), gives the equilibrium moments

$$\begin{aligned}
A_{10} &= \frac{u_N}{u}(\frac{\cos\theta''}{\rho_i} + \frac{\rho_e}{\cos\theta''})A_{00}, \\
A_{20} &= \frac{2T}{eBu\sin\theta''}A_{00}, \\
A_{30} &= 0, \text{ and for } l > 3 \\
A_{l0} &= \frac{2T}{eBu\sin\theta''}(l-1)A_{(l-2)0}, \qquad (17)
\end{aligned}$$

where Λ_i has been set to 1 in the final result. It can be verified that the moments (17) also determine the Gaussian profile Eq. (8) with Eq. (9).

To analyze the stability of the system, consider perturbative deformations

$$\begin{aligned}
&A_l = A_{l0} + \delta A_l,\ \boldsymbol{E} = \boldsymbol{E}_0 + \hat{y}'\delta E_{y'},\ \text{with} \\
&\delta A_l = \Delta A_l \mathrm{e}^{iky'},\ \delta E_{y'} = \tilde{E}\mathrm{e}^{iky'}, \qquad (18)
\end{aligned}$$

where A_{l0} is given by Eq. (17), $\boldsymbol{E}_0$ is given by Eq. (6), and we will assume that the polarization electric field $\delta E_{y'}$ maps unattenuated along $\boldsymbol{B}$ in the region of significant E_s density. It was argued in Sect. 4.1 that $\delta E_{y'}$ must be in the $\hat{y}'$ direction. To determine $\tilde{E}$ we consider the zeroth moment of the current continuity condition

$$\begin{aligned}
\int \mathrm{d}z'\, \nabla\cdot\boldsymbol{J} &= J_\parallel + \int \mathrm{d}z'\, \nabla_\perp\cdot\boldsymbol{J} \\
&= J_\parallel + \frac{\partial}{\partial y'}\int \mathrm{d}z'\, J_{y'} = 0, \qquad (19)
\end{aligned}$$

where $\boldsymbol{J}$ is the current density carried by the E_s layer plasma, and $J_\parallel$ is the current flowing up the magnetic field lines, connecting the E_s layer with the F layer. To get $J_\parallel$ we use the results of Cosgrove and Tsunoda (2004b) to compute the loading conductance Σ_L seen by the E_s layer, due to the F layer, such that

$$J_\parallel = \int \mathrm{d}z' \, \nabla_\perp \cdot \boldsymbol{J}_F = \frac{\partial}{\partial y'} \int \mathrm{d}z' \, J_{Fy'} = \frac{\partial}{\partial y'} \delta E_{y'} \Sigma_L, \quad (20)$$

where $\boldsymbol{J}_F$ is the current density carried by the F layer plasma, caused by partial mapping of $\delta E_{y'}$ to the F layer. Simple circuit theory applied to the circuit model given in Fig. 5 of Cosgrove and Tsunoda (2004b) gives

$$\Sigma_L = \frac{1}{2R_0 + R_F} = \frac{1}{k^2 \int_B \frac{1}{\sigma_0} + \frac{1}{\Sigma_{PF}}}, \quad (21)$$

where Σ_{PF} is the field line integrated F layer Pedersen conductivity, σ_0 is the field aligned conductivity, and $\int_B$ denotes integration along the magnetic field line between the E_s layer and the F layer. (Although the top of the integration range may seem somewhat ill defined, the integral is dominated by the low altitude contribution, where the boundaries are well defined.)

Subtracting the electron velocity from the ion velocity gives the the usual Ohms law, which in the polarization electric field aligned direction appears as

$$\begin{aligned} J_{y'} &= en(v_{iy'} - v_{ey'}) \\ &= n(E_{x'} + u_{y'}B)\sigma_H + n(E_{y'} - u_{x'}B)\sigma_P \\ &\quad + T(\alpha_H \frac{\partial n}{\partial x'} + \alpha_P \frac{\partial n}{\partial y'}), \quad \text{where} \\ \sigma_P &= \frac{e}{B}\frac{\rho_e}{1+\rho_e^2} + \frac{e}{B}\frac{\rho_i}{1+\rho_i^2}, \\ \sigma_H &= \frac{e}{B}\frac{1}{1+\rho_e^2} - \frac{e}{B}\frac{1}{1+\rho_i^2}, \end{aligned} \quad (22)$$

$n\sigma_P$ is the Pedersen conductivity, $n\sigma_H$ is the Hall conductivity, and in the altitude range of interest $\alpha_P \simeq -\sigma_P/e$, and $\alpha_H \simeq \sigma_H/e$. Substituting Eqs. (22), (20), (18), and (6) into Eq. (19) and solving for $\tilde{E}$ gives

$$\begin{aligned} \tilde{E} &= -uB(\sigma_P \sin\theta' + \sigma_H \cos\theta')\frac{\Delta A_1}{\Sigma_{PE} + \Sigma_L} \\ &\quad + u_N B(\sigma_P \cos\theta' \cos\theta'' - \sigma_H \sin\theta' \cos\theta'')\frac{\Delta A_0}{\Sigma_{PE} + \Sigma_L} \\ &\quad + i\frac{2Tk}{e}\sigma_P \frac{\Delta A_0}{\Sigma_{PE} + \Sigma_L}, \end{aligned} \quad (23)$$

where a term smaller by a factor of ρ_e has been dropped, and $\Sigma_{PE} = \sigma_P A_{00}$ is the equilibrium field line integrated conductivity of the E_s layer. Substituting the velocity expressions (14), the moment relations (15), the perturbative deformations (18) with Eq. (17), and the electric field expressions (6) and (23) into the time derivative expression (13), and keeping only the first order terms, gives the linearized equations of motion

$$\frac{\mathrm{d}\Delta A_l}{\mathrm{d}t} = \sum_{m=0}^{l+1} M_l^m \Delta A_m, \quad (24)$$

where the elements M_l^m of the matrix $\mathbf{M}$ are constants. If the system were closed, that is, if $M_k^l = 0$ for $k < l$, for some l, then the system growth rates would be the real parts of the eigenvalues of the square matrix $\mathbf{M}$, and the associated growing modes would be the eigenvectors.

However, the system (24) is not closed in general. Cosgrove and Tsunoda (2002) obtained a closed system by assuming an infinitely thin layer, so that $A_2 = 0$. This is appropriate when the wavelength is much greater than the layer thickness. Here, a less drastic approximation is desired, so that the thick layer effects that determine the short wavelength cutoff of the E_s layer instability will be accounted for.

In general there is no justification for setting $A_l = 0$ for some l, and the system is not closed. Instead, we will follow the approach commonly used to close the system of fluid equations derived from kinetic theory. Specifically, the E_s layer profile will be expanded about a Gaussian as a sum of Hermite polynomials:

$$\begin{aligned} n &= n_1 \sum_{m=0}^{N} H_m(b(z - \bar{z}))\alpha_m, \ \text{where} \\ n_1 &= A_{00}\frac{b}{\sqrt{\pi}} \mathrm{e}^{-b^2(z-\bar{z})^2}, \\ \alpha_1 &= 0, \ \text{and otherwise } \alpha_m = \alpha_m(y'). \end{aligned} \quad (25)$$

The stipulation $\alpha_1 = 0$ is made so that $\bar{z}$ can be used to define A_1, consistent with Eq. (10). The notation $\alpha_m = \alpha_m(y')$ indicates that α_m is a function of y' only, so that Eq. (25) defines the profile along lines perpendicular to $\hat{y}'$.

Because $H_0 = 1$, the expansion (25) reduces to a Gaussian when $\{\alpha_m = 0 | m > 0\}$. The Hermite polynomials $H_m(x)$ satisfy the orthogonality relation

$$\int_{-\infty}^{\infty} \mathrm{d}x \, \mathrm{e}^{-x^2} H_m(x) H_n(x) = n! \, 2^n \sqrt{\pi} \, \delta_{nm}. \quad (26)$$

The completeness of Hermite polynomials, combined with the orthogonality relation (26), provide a canonical polynomial expansion about a Gaussian layer profile. It is physically reasonable to model the layer by the expansion (25) for some finite N. Doing this defines a representation of the moment A_{N+1} in terms of a linear combination of lower order moments. Because the relationship is linear, it applies also to the moment perturbations ΔA_l, thus closing the linear system (24) in a physically reasonable way.

Specifically, write $(z - \bar{z}h_{K1})^K$ in terms of a sum of Hermite polynomials:

$$(z - \bar{z}h_{K1})^K = \sum_{n=0}^{K} H_n(b(z - \bar{z}))B_K^n. \quad (27)$$

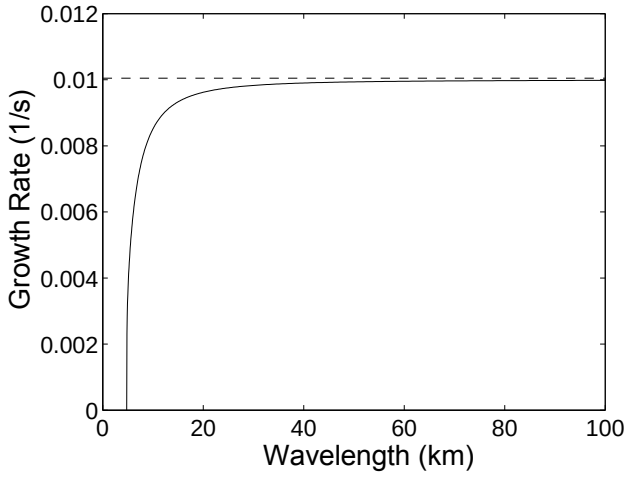

Fig. 2. E_s layer instability growth rate as a function of wavelength for 1/2 km thick layer, without F region loading (solid line). The dashed line shows the growth rate computed from the formula given by Cosgrove and Tsunoda (2002).

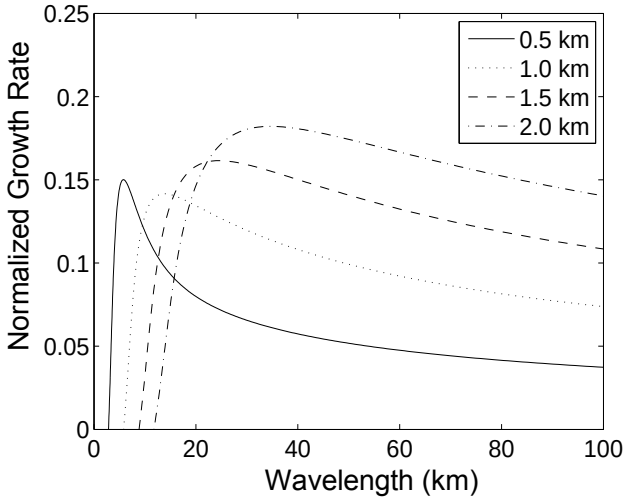

Fig. 3. E_s layer instability growth rate as a function of wavelength for 1/2 km thick layer, with wavelength dependent F region loading.

Substituting Eqs. (27) and (25) into the moment definition (10) and using the orthogonality relation (26) gives

$$A_K = \sum_{m=0}^{N} M_K^m \alpha_m, \text{ where}$$

$$M_K^m = B_K^m \frac{m!\, 2^m A_{00}}{\cos\theta''}, \; M_K^m = 0 \text{ for } m > K, \tag{28}$$

which is valid for any K. Therefore, defining the $N \times N$ matrix $\mathbf{D}$ with elements $D_l^m = M_l^m$, the length N vector $\boldsymbol{A}$ with elements A_l, and the length N vector $\boldsymbol{\alpha}$ with elements α_l, gives the invertible relation

$$\boldsymbol{A} = \mathbf{D}\boldsymbol{\alpha}. \tag{29}$$

Inverting Eq. (29) and substituting into Eq. (28) with $K = N+1$ gives

$$A_{N+1} = \sum_{m=0}^{N} \sum_{l=0}^{N} M_{N+1}^m [\mathbf{D}^{-1}]_m^l A_l. \tag{30}$$

The linear relation (30) will be used to close the linearized equations of motion (24) at the Nth moment. In practice, we close the system after 14 moments, which is more than sufficient for convergence. As mentioned above, the real parts of the eigenvalues of the resulting system are the linear growth rates.

5 Results

The results for the growth rate as a function of wavelength when the F layer loading effect is ignored ($\Sigma_{PF}=0$) are shown in Fig. 2 (solid line), together with the growth rate computed using the simple analytical expression (2) (dashed line). It is normally not a good approximation to ignore F layer loading, and this figure is mainly for the purposes of comparing the result of the derivation given here with that of Cosgrove and Tsunoda (2002). The parameters T=230 °k, ρ_i=24, σ_H/σ_P=21, θ'=45°, and θ''=45° are used in all figures in this paper. Figure 2 employs the additional choices u=32 m/s/km, and Σ_{PF}=0. When Σ_{PF}=0, the value for A_{00} cancels out of the growth rate expression. Figure 2 shows that the growth rate matches Eq. (2) very well down to a wavelength of about 20 km, below which it drops off precipitously, becoming zero at about 5 km. When $u_N > 0$ (and Σ_{PF}=0) the curve (not shown) is nearly identical with that in Fig. 2, but is not strictly below the value computed from the simple analytical expression. The effect of u_N on the linear growth rate is insignificant when Σ_{PF}=0, but becomes very important for realistic values of Σ_{PF}.

The effect of wavelength dependent F layer loading is shown in Fig. 3. The parameters for the solid curve in Fig. 3 are the same as in Fig. 2, except Σ_{PF}=0.23 mhos, Σ_{PE}=0.021 mhos, and $1/\int_B \frac{1}{\sigma_0} = 8.95\times10^{-8}$ mhos/m^2. The growth rate has been normalized by the wind shear in units of s^{-1}, that is by 0.032. As the wavelength decreases the F layer loading decreases, according to Eq. (21), leading to a growth rate maxima at a wavelength of about 6 km, just above where the growth rate plunges to zero. The wind shear u=32 m/s/km creates a 500 m thick equilibrium E_s layer. (By layer thickness we mean the value that when multiplied by the peak density, gives the height integrated density.) This rather thin layer allows relatively short wavelength (5 km) modes of the E_s layer instability.

The short wavelength cutoff of the instability occurs because when the wavelength becomes comparable to the layer

thickness, the effective geometry is no longer that of an infinitely thin layer. To investigate the dependence of the cutoff wavelength on layer thickness, the growth rate normalized by the wind shear (in units of s^{-1}) is plotted in Fig. 3, for layer thicknesses of 500 m, 1 km, 1.5 km, and 2 km. The layer thickness is varied by varying the wind shear. The F region and field aligned parameters are kept the same. By Eq. (2), the growth rate for an infinitely thin layer is proportional to the wind shear, so that normalizing by the wind shear provides quantities that can be compared with respect to the wave length dependence caused by the thickness of the layer. Figure 3 shows that for layers of thickness 500 m, 1 km, 1.5 km, and 2 km, the maximum growth rate occurs at wavelengths of 6 km, 14 km, 25 km, and 34 km, respectively.

For reference, the equilibrium layer thickness is plotted versus wind shear in Fig. 6. The wind shears used in Fig. 3 are 32 m/s/km, 8 m/s/km, 3.6 m/s/km, and 2.0 m/s/km. The associated minimum e-folding times (inverse of growth rate maxima) are 3.5 min, 15 min, 29 min, and 46 min, respectively. It is interesting to note that an e-folding time of, for example, 29 min, which occurs for a wind shear of only 3.6 m/s/km, is not prohibitively long.

While some of the wind sheers used are very small, we have elected to present the results in Fig. 3 organized by layer thickness out of the belief that it is the layer thickness, and not the wind shear, which is the fundamental determiner of the wavelength dependence. That is, in a realistic situation where the layer may not be in equilibrium, because instability growth occurs before equilibrium is achieved, or due to time dependence of the wind shear node altitude (Jones, 1989), or of the wind shear strength, or if there is some sort of anomalous diffusion process, etc., then the layer may be substantially thicker than the equilibrium value computed here. In such cases we expect the layer thickness, and not the instantaneous wind shear, to determine the wavelength dependence of the electrodynamical response.

In Fig. 4 the growth rate is plotted versus the layer thickness for two different wavelengths, 5 km and 25 km. Other parameters are the same as stated above. The result shows that although the growth rate for 5 km waves is quite a bit larger than the growth rate for 25 km waves when the layer thickness is 500 m or less, the reverse becomes true as the layer gets thicker. In fact, 5 km waves are stabilized when the layer thickness exceeds about 900 m, while 25 km waves maintain a substantial growth rate for much thicker layers. Given the fact that actual E_s layers may not often be in thermal equilibrium, such as discussed in the previous paragraph, this suggests that 5 km may be a significant underestimate of the realistic preferred wavelength of the E_s layer instability, in spite of the fact that instantaneous wind shears of 32 m/s/km (500 m equilibrium thickness) are frequently observed (Larsen et al., 1998; Larsen, 2002). Therefore, although not predictive, the results here are consistent with the 17 km mean wavelength associated with QP echoes, and with the 24 km mean wavelength associated with spaced

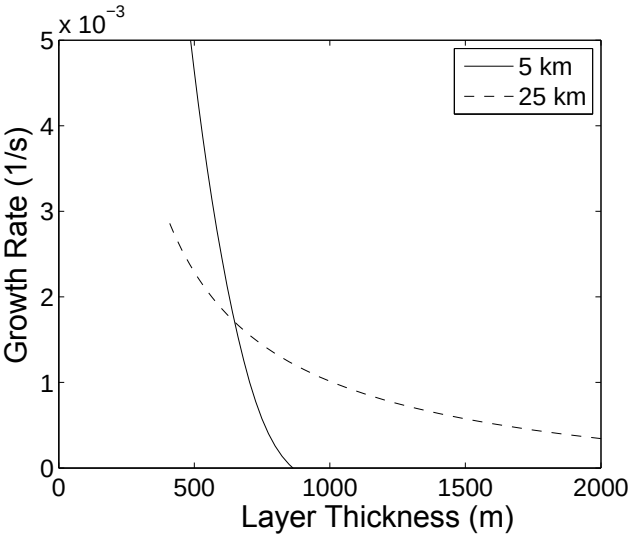

Fig. 4. E_s layer instability growth rate as a function of layer thickness, with wavelength dependent F region loading, for wavelengths of 5 km and 25 km.

ionosonde measurements of frontal structures, such as discussed in the introduction. We also note that if a physical process with a well defined wavelength is involved in initiating the growth of unstable waves, then this "seeding" mechanism will be an important determiner of the observed wavelength.

Figure 5 shows contour plots of the 25 km wavelength growth rate verses $\Sigma_H/(\Sigma_{PE}+\Sigma_L)$, and southward wind, where the latter is represented by the effective eastward electric field $E'_{y''}$, which in this case equals $-u_N B \cos\theta'$. (Use of $E'_{y''}$ allows generalization of the results, because in general the growth rate depends on the zeroth order meridional Hall current in the E_s layer, whether it is driven by a southward wind, an eastward electric field, or any combination thereof (Cosgrove and Tsunoda, 2004a).) Panel (a) shows the results for a 1 km thick layer, and panel (b) for a 500 m thick layer. Other parameters are maintained as above. Figure 5 shows some threshold conditions for the E_s layer instability. Especially, it shows the importance of the effective eastward electric field at the E_s layer altitude $E'_{y''}$ in destabilizing the layer. In fact, for the fairly large ratio $\Sigma_H/(\Sigma_{PE}+\Sigma_L)$=3, the layer is stable if $E'_{y''}$=0. This indicates that the simple physical description of the E_s layer instability given in Sect. 3 is overly simplified, because it considers only altitude modulation, and omits FLI density modulation. The latter generates polarization fields when there is a zeroth order meridional current (generated by $E'_{y''}$), which leads to an interaction with altitude modulations.

The equivalence between winds and electric fields can be used to generalize the results to conditions involving background electric fields. The "effective" electric field is

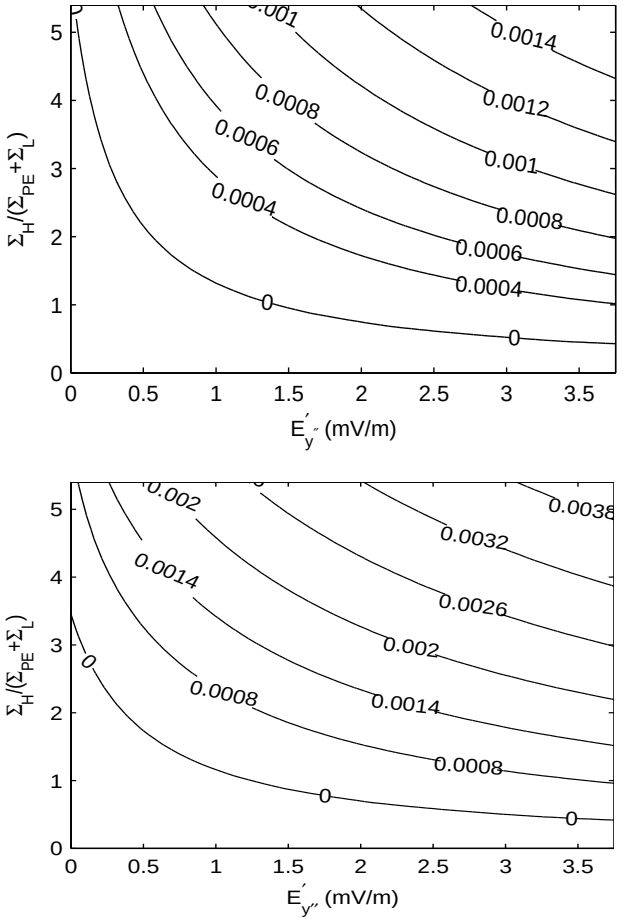

Fig. 5. Contour plot of the E_s layer instability growth rate as a function of the meridional wind u_N, and of the integrated conductivity ratio $\Sigma_H/(\Sigma_{PE}+\Sigma_L)$, for a 25 km wavelength. Panel **(a)** is for a 1 km thick layer, and panel **(b)** for a 1/2 km thick layer. The growth rate contour lines are labeled in units of $1/s$. Stable regions are seen below the contour lines labeled 0.

$\boldsymbol{E}'=\boldsymbol{E}+\boldsymbol{u}\times\boldsymbol{B}$, where $\boldsymbol{u}$ is the neutral wind velocity. As long as the effective electric field and the shear in effective electric field are the same, then the layer response will be the same, up to an overall horizontal velocity offset. The equilibrium altitude will be at the zero of the meridional component of the effective electric field. (These conclusions follow under the assumption that all winds are horizontal.)

The choices for the field line integrated F layer conductivity, and field aligned conductivity profile, were made by appealing to the International Reference Ionosphere (IRI) (Bilitza, 1990) and COSPAR International Reference Atmosphere (CIRA) (Rees, 1988) models. To do this the web cite maintained by the World Data Center, Kyoto, was used, which outputs the integrated conductivity as a function of season, sunspot number, latitude, longitude, etc. The numbers Σ_{PF}=0.23 mhos and $1/\int_B \frac{1}{\sigma_0}$=$8.95\times10^{-8}$ mhos/m^2

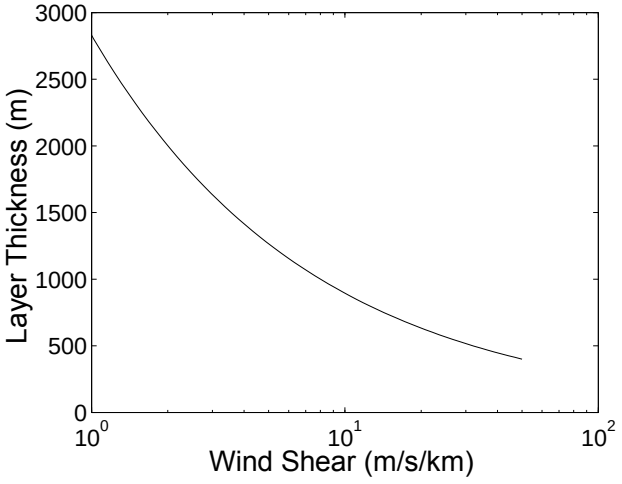

Fig. 6. Equilibrium E_s layer thickness versus wind shear.

are representative of summertime with low solar activity. For the E_s layer integrated conductivity we assumed a 1 km thick layer with a density of 10^{11} m^{-3}, which gives a total electron content (TEC) of 10^{14} m^{-2}. This choice is motivated by Figs. 7 and 8 from Miller and Smith (1978), who compiled E_s layer statistics from high resolution incoherent scatter measurements made by the Arecibo observatory. In addition, Wakabayashi et al. (2005) computed the TEC from impedance probe measurements made during the SEEK2 rocket campaign, and found values exceeding 10^{14} m^{-2} for both rockets. Using ρ_i=24 and B=4.4×10^{-5} T gives Σ_{PE}=0.021 mhos.

6 Summary of conclusions and results

This work contains the following conclusions and results with respect to the E_s layer instability:

1. The linear growth rate has a short wavelength cutoff that increases as the equilibrium layer thickness increases, or equivalently, as the background wind shear decreases.

2. The wavelength that maximizes the linear growth rate also increases as the layer thickness increases.

3. The large wind shears that have often been observed by rockets would, under the idealized conditions assumed here, lead to layer thicknesses of 500 m or less, and growth rate maxima at wavelengths somewhat shorter than normally observed (∼6 km).

4. However, with respect to item 3, we conjecture that E_s layers do not normally achieve equilibrium, and hence are thicker than expected from the instantaneous wind shear.

5. We further argue that the layer thickness is the salient feature in determining the wavelength dependence of the electrodynamical response, and that therefore the nonequilibrium layer thickness conjecture leads to the observed wavelengths of E_s layer fronts.

6. A three-dimensional paper model has been used to describe the geometry of the instability, and to give a more visual restatement of the physical mechanism originally described by Cosgrove and Tsunoda (2002).

7. The role of FLI conductivity modulation ($E'_{y''}$) has been reexamined, in light of the result in Cosgrove and Tsunoda (2004a), and found to be one of critical importance to the E_s layer instability. This means that the description of the physical mechanism of instability given in Sect. 3, although of pedagogical significance, is incomplete, and should be augmented by a notion of coupling between altitude modulations and FLI-density modulations.

The results are derived within the framework of the linear growth rate of the E_s layer instability, which by definition assumes an initial equilibrium configuration, and which has diminishing relevance when the background conditions are time-varying (Jones, 1989), and/or when evolution proceeds into the nonlinear regime. Although it is difficult to study these complicating effects in general, simulations can be used to study specific, judiciously chosen examples. Work of this sort is underway, in order to verify the relevance of the above results. The reader is referred to Cosgrove and Tsunoda (2003), and Cosgrove (2007)[1] for numerical simulations of the E_s layer instability.

Acknowledgements. This material is based upon work supported by the National Science Foundation under Grant No. 0436568. The author thanks R. Tsunoda for valuable discussions, and V. Moore who conceived of and produced the paper model in Fig. 1.

Topical Editor M. Pinnock thanks Y. Dimant and M. Larsen for their help in evaluating this paper.

References

Bernhardt, P. A.: The modulation of sporadic-*E* layers by Kelvin-Helmholtz billows in the neutral atmosphere, J. Atmos. Solar Terr. Phys., 105, 1487–1504, 2002.

Bilitza, D.: International Reference Ionosphere, National Space Science Data Center/World Data Center-A for Rockets and Satellites, 1990.

Cosgrove, R. B. and Tsunoda, R. T.: A direction-dependent instability of sporadic-*E* layers in the nighttime midlatitude ionosphere, Geophys. Res. Lett., 29(18), 1864–1867, 2002.

[1]Cosgrove, R. B.: Generation of mesoscale *F* layer structure and electric fields by the combined Perkins and E_s layer instabilities, in simulations, Ann. Geophys., submitted, 2007.

Cosgrove, R. B. and Tsunoda, R. T.: Simulation of the nonlinear evolution of the sporadic-*E* layer instability in the nighttime midlatitude ionosphere, J. Geophys. Res., 108(A7), 1283, doi:10.1029/2002JA009728, 2003.

Cosgrove, R. B. and Tsunoda, R. T.: Instability of the *E*-*F* coupled nighttime midlatitude ionosphere, J. Geophys. Res., 109, A04305, doi:10.1029/2003JA010243, 2004a.

Cosgrove, R. B. and Tsunoda, R. T.: Coupling of the Perkins instability and the sporadic *E* layer instability derived from physical arguments, J. Geophys. Res., 109, A06301, doi:10.1029/2003JA010295, 2004b.

Goodwin, G. L. and Summers, R. N.: E_s layer characteristics determined from spaced ionosondes, Planet Space Sci., 18, 1417–1432, 1970.

Huang, C. and Kelley, M. C.: Numerical simulation of gravity wave modulation of midlatitude sporadic *E* layers, J. Geophys. Res., 101(A11), 24 533–24 543, 1996.

Hysell, D. L., Yamamoto, M., and Fukao, S.: Simulations of plasma clouds in the midlatitude *E* region ionosphere with implications for Type I and Type II quasiperiodic echoes, J. Geophys. Res. 107(A10), 1313, doi:10.1029/2002JA009291, 2002.

Hysell, D. L.: Presentation at the CEDAR workshop in Santa Fe, New Mexico, 2006.

Jones, K. L.: Mechanisms for vertical separation of ions in sporadic-*E* layers, J. Atmos. Terr. Phys., 51(6), 469–476, 1989.

Kelley, M. C. and Gelinas, L. J.: Gradient drift instability in midlatitude sporadic *E* layers: localization of physical and wavenumber space, Geophys. Res. Lett., 27(4), 457–460, 2000.

Larsen, M. F., Fukao, S., Yamamoto, M., Tsunoda, R., Igarashi, K., and Ono, T.: The SEEK chemical release experiment: Observed neutral wind profile in a region of sporadic *E*, Geophys. Res. Lett., 25, 1789–1792, 1998.

Larsen, M. F.: A shear instability seeding mechanism for quasiperiodic radar echoes, J. Geophys. Res. 105, 24 931–24 940, 2000.

Larsen, M. F.: Winds and shears in the mesosphere and lower thermosphere: Results from four decades of chemical release wind measurements, J. Geophys. Res., 107(A8), 1215, doi:10.1029/2001JA000218, 2002.

Miller, K. L. and Smith, L. G.: Incoherent scatter radar observations of irregular structure in midlatitude sporadic-E layers, J. Geophys. Res., 83, 3761–3775, 1978.

Mori, H. and Oyama, K.: Sounding rocket observation of sporadic-E layer electron-density irregularities, Geophys. Res. Lett. 25(11), 1785–1788, 1998.

Perkins, F.: Spread *F* and ionospheric currents, J. Geophys. Res., 78, 218–226, 1973.

Pfaff, R., Yamamoto, M., Marionni, P., Mori, H., and Fukao, S.: Electric field measurements above and within a sporadic-*E* layer, Geophys. Res. Lett. 25, 1769–1772, 1998.

Pfaff, R., Freudenreich, H., Yokoyama, T., Yamamoto, M., Fukao, S., Mori, H., Ohtsuka, S., and Iwagami, N.: Electric field measurements of DC and long wavelength structures associated with sporadic-*E* layers and QP radar echoes, Ann. Geophys., 23, 2319–2334, 2005, http://www.ann-geophys.net/23/2319/2005/.

Rees, D.: COSPAR international reference atmosphere: 1986 part I: Thermosphere models, Adv. Space Res., 8(5–6), 27–106, Pergamon Press, 1988.

Riggin, D., Swartz, W. E., Providakes, J., and Farley, D. T.: Radar studies of long-wavelength waves associated with midlatitude sporadic E layers, J. Geophys. Res., 91, 8011–8024, 1986.

Rosado-Roman, J. M., Swartz, W. E., and Farley, D. T.: Plasma instabilities observed in the *E* region over Arecibo and a proposed nonlocal theory, J. Atmos. Solar Terr. Phys., 66, 1593–1602, 2004.

Schlegel, K. and Haldoupis, C.: Observation of the modified two-stream plasma instability in the midlatitude *E* region ionosphere, J. Geophys. Res. 99, 6219–6226, 1994.

Seyler, C. E., Rosado-Roman, J. M., and Farley, D. T.: A nonlocal theory of the gradient-drift instability in the ionospheric *E*-region plasma at midlatitudes, J. Atmos. Solar Terr. Phys., 66, 1627–1637, 2004.

Tsunoda, R., Fukao, S., and Yamamoto, M.: On the origin of quasi-periodic radar backscatter from midlatitude sporadic *E*, Radio Sci. 29, 349–365, 1994.

Tsunoda, R. T., Fukao, S., Yamamoto, M., and Hamasaki, T.: First 24.5-MHz radar measurements of quasi-periodic backscatter from field-aligned irregularities in midlatitude sporadic *E*, Geophys. Res. Lett., 25(11), 1765, 1998.

Tsunoda, R. T., Cosgrove, R. B., and Ogawa, T.: Azimuth-dependent E_s layer instability: A missing link found, J. Geophys. Res., 109, A12303, doi:10.1029/2004JA010597, 2004.

Wakabayashi, M., Ono, T., Mori, H., and Bernhard, P. A. T.: Electron density and plasma waves in mid-latitude sporadic-*E* layer observed during the SEEK-2 campaign, Ann. Geophys., 23, 2335–2345, 2005, http://www.ann-geophys.net/23/2335/2005/.

Whitehead, J. D.: Report on the production and prediction of sporadic-*E*, Rev. Geophys. Space Phys., 8, 65–144, 1970.

Yamamoto, M., Fukao, S., Woodman, R. F., Ogawa, T., Tsuda, T., and Kato, S.: Midlatitude *E*-region field-aligned irregularities observed with the MU radar, J. Geophys. Res. 96, 15 943–15 949, 1991.

Yamamoto, M., Komoda, N., Fukao, S., Tsunoda, R., Ogawa, T., and Tsuda, T.: Spatial structure of the *E* region field-aligned irregularities revealed by the MU radar, Radio Sci., 29(1), 337, 1994.

Yamamoto, M., Fukao, S., Tsunoda, R. T., Igarashi, K., and Ogawa, T.: Preliminary results from joint measurements of E-region field-aligned irregularities using the MU radar and the frequency-agile radar, J. Atmos. Solar Terr. Phys., 59, 1655–1663, 1997.

Yamamoto, M., Itsuki, T., Kishimoto, T., Tsunoda, R. T., Pfaff, R. F., and Fukao, S.: Comparison of *E*-region electric fields observed with a sounding rocket and a Doppler radar in the SEEK campaign, Geophys. Res. Lett. 25, 1773, 1998.

Yamamoto, M., Fukao, S., Tsunoda, R. T., Pfaff, R., and Hayakawa, H.: SEEK-2 (sporadic-E experiment over Kyushu 2)-project outline, and significance, Ann. Geophys., 23, 2319–2334, 2005, http://www.ann-geophys.net/23/2319/2005/.

Yokoyama, T. Horinouchi, Yamamoto, M., and Fukao, S.: Modulation of the midlatitude ionospheric E region by atmospheric gravity waves through polarization electric field, J. Geophys. Res. 109, A12307, doi:10.1029/2004JA010508, 2004.